npj computational materials

www.nature.com/npjcompumats

ARTICLE OPEN

Check for updates

# Discovering plasticity models without stress data

Moritz Flaschel[1], Siddhant Kumar[2] and Laura De Lorenzis[1]✉

We propose an approach for data-driven automated discovery of material laws, which we call EUCLID (Efficient Unsupervised Constitutive Law Identification and Discovery), and we apply it here to the discovery of plasticity models, including arbitrarily shaped yield surfaces and isotropic and/or kinematic hardening laws. The approach is *unsupervised*, i.e., it requires no stress data but only full-field displacement and global force data; it delivers *interpretable* models, i.e., models that are embodied by parsimonious mathematical expressions discovered through sparse regression of a potentially large catalog of candidate functions; it is *one-shot*, i.e., discovery only needs one experiment. The material model library is constructed by expanding the yield function with a Fourier series, whereas isotropic and kinematic hardening is introduced by assuming a yield function dependency on internal history variables that evolve with the plastic deformation. For selecting the most relevant Fourier modes and identifying the hardening behavior, EUCLID employs physics knowledge, i.e., the optimization problem that governs the discovery enforces the equilibrium constraints in the bulk and at the loaded boundary of the domain. Sparsity promoting regularization is deployed to generate a set of solutions out of which a solution with low cost and high parsimony is automatically selected. Through virtual experiments, we demonstrate the ability of EUCLID to accurately discover several plastic yield surfaces and hardening mechanisms of different complexity.

*npj Computational Materials* (2022)8:91 ; https://doi.org/10.1038/s41524-022-00752-4

## INTRODUCTION

Data-driven and machine-learning-based methods are currently pushing forward the frontiers of material modeling. What started with simple regression on uniaxial tensile data has rapidly expanded into high-dimensional and big-data-based surrogate modeling of basically all types of materials of technical interest, including metals, polymers, composites, and more. While conventional material modeling was based on the a priori assumption of a constitutive law of which the unknown parameters were identified through best-fitting with experimental (or, within multiscale settings, lower-scale computational) results, current data-driven and machine-learning methods give up the usage of an analytical constitutive law altogether. In doing so, they avoid the modeling errors arising due to, e.g., the largely experience-based modeling assumptions and the choice of experimental (or computational) tests being too restrictive to describe the true physics.

Despite the achieved progress, currently available methods are still problematic due to their data-hungry and black-box nature. The state-of-the-art techniques[1–9] that either *bypass* (directly use data as look-up tables in a model-free fashion) or *surrogate* (encode in, e.g., artificial neural networks (ANNs) or Gaussian processes) material models are rooted in a *supervised learning* or *curve-fitting* setting. Hence, they need a large amount of data consisting of input–output, i.e., strain-stress pairs. Since experimental stress data are only obtainable in the simplest situations, e.g., uniaxial tensile or bending tests, the comprehensive observation of strain-stress relations relying on these tests is nearly impossible. Additionally, stress tensors are challenging to measure experimentally, while force measurements only provide incomplete data in the form of boundary-averaged projections of stress tensors. Multiscale simulations can generate training data sets with tensorial stress–strain pairs, but their computational cost is still too expensive to probe the entire high-dimensional stress–strain space. Recognition of this issue is very recent. Within the constitutive-model-free paradigm, it motivated the development of the data-driven identification method[10,11], which formulates the inverse problem associated with the approach in ref. [3]. Likewise recognizing the issue of limited stress data availability, a mathematical framework is proposed in ref. [12] to calculate stress fields from deformation fields under the assumption of the alignment of the principal directions of stress and strain or strain rate. Within the stream of research on surrogating constitutive models with ANNs, recent attempts to use only displacement and global force data have been performed[13–15], but are limited to very simple cases (constitutive models of known form with unknown parameters or unknown constitutive models but for one-dimensional cases). At last, the *uninterpretability* of stress–strain relations in both paradigms is a standing challenge: it implies significant difficulties in enforcing or verifying the satisfaction of physics constraints and it hinders the extrapolation power.

From the perspectives of both the labeled data requirement and uninterpretability, the treatment of path-dependent material behavior, such as plasticity, is even more challenging as the stress state at a material point is not solely defined by its strain state, but is additionally dependent on the history of that material point, which is traditionally described using internal variables. Also in this context, the idea of constitutive-model-free approaches is to bypass the formulation of a path-dependent constitutive law and hence any assumptions on the material behavior, by solving forward problems that are directly informed by the given data [16–21]. The other stream of approaches describes the path-dependent constitutive behavior based on ANNs[7,22–27], support vector machines[28], symbolic regression[29], or use the information gained from the data to correct material models known from traditional theories[30]. Being *supervised*, all these methods require for the training process a tremendous amount of labeled data in

[1]Department of Mechanical and Process Engineering, ETH Zürich, 8092 Zürich, Switzerland. [2]Department of Materials Science and Engineering, Delft University of Technology, 2628 CD Delft, The Netherlands. ✉email: ldelorenzis@ethz.ch

form of stress–strain *paths*, i.e. stress–strain couples at each time over each possible loading history. In other words, it is no longer sufficient to sample data from the stress–strain space; instead, stress–strain *increments* for several - theoretically infinite - loading histories are required. This makes the coverage of the sampling space basically impossible and the supervised learning task unfeasible. This conclusion applies regardless of whether the data are meant to come from experiments (in which case, as mentioned earlier, already path-independent sampling is highly problematic) or from multiscale simulations (whose computational cost, which is already prohibitive in the path-independent case, becomes now orders of magnitude larger).

In this light, we propose EUCLID (Efficient Unsupervised Constitutive Law Identification and Discovery), an *unsupervised* discovery framework that bridges the advantages of data-driven and traditional modeling approaches. EUCLID does not require the a priori choice of a material model and thus is flexible to describe a variety of different material behaviors, and it only relies on unlabeled data, i.e., full-field displacements (obtained e.g., via Digital Image Correlation (DIC)) and global reaction forces but no stress data, generated by a *single experiment*. EUCLID was recently successfully demonstrated for hyperelastic material model discovery[31–33] and is here extended to the significantly more challenging problem of path-dependent elastoplasticity. The idea is to formulate a large library of *interpretable* candidate material models (also referred to as features) and to automatically discover the most relevant features in the library based on the given unlabeled data using only physics constraints (as opposed to stress labels). The inspiration for this approach comes from the dynamics community, where sparse regression from a library of candidate features has been used to discover the nonlinear dynamics of physical systems[34], albeit in a strictly supervised setting.

Our objective here is to discover fully general and evolving plastic yield surfaces, which characterize the material behavior of three-dimensional elastoplastic solids, purely based on two-dimensional displacement field and reaction force measurements from only one experimental test on an arbitrarily shaped specimen. The material model library is constructed by expanding the yield function with a Fourier series containing a potentially large number of terms. Yield surface growth and translation, i.e., isotropic and kinematic hardening, are introduced by making the yield function dependent on the accumulated plastic multiplier and the back stress, which are internal history variables that evolve with the plastic deformation. For selecting the most relevant Fourier modes and identifying the hardening mechanisms, EUCLID employs physics knowledge, i.e., the optimization problem that governs the discovery is formulated based on the balance of linear momentum, compensating for the unavailability of stress data. The step-by-step schematic of EUCLID is illustrated in Fig. 1 and described below.

## RESULTS

### Material model library

In this work on path-dependent material behavior, we focus on homogeneous, isotropic materials for which linear elastic behavior is followed by associated, pressure-insensitive plastic behavior with isotropic and/or kinematic hardening. We also assume small strains and plane stress conditions. In the theory of elastoplasticity, the infinitesimal strain tensor, which is obtained from the spatial gradient of the displacement field $\mathbf{u}$, is additively split into an elastic contribution and a plastic contribution $\boldsymbol{\epsilon} = \boldsymbol{\epsilon}_\mathrm{e} + \boldsymbol{\epsilon}_\mathrm{p}$, with the plastic strain acting as internal (or history) variable. The elastic properties of the material are characterized by the stiffness tensor $\mathbb{C}$, which determines the linear relation between the elastic strain and the Cauchy stress tensor $\boldsymbol{\sigma} = \mathbb{C} : \boldsymbol{\epsilon}_\mathrm{e}$, whereas the plastic properties are described through the yield function $f(\boldsymbol{\sigma}, \gamma, \boldsymbol{\sigma}^\mathrm{back})$, which is here assumed to be dependent on the stress tensor, the accumulated plastic multiplier $\gamma$, and the back stress tensor $\boldsymbol{\sigma}^\mathrm{back}$. The zero level set $f = 0$ defines the yield surface, i.e., the material deforms elastically if $f < 0$, and plastic yielding occurs at $f = 0$. Further, the yield function governs the evolution of the plastic strain through the plastic evolution law

$$\dot{\boldsymbol{\epsilon}}_p = \dot{\gamma} \frac{\partial f(\boldsymbol{\sigma}, \gamma, \boldsymbol{\sigma}^\mathrm{back})}{\partial \boldsymbol{\sigma}}, \tag{1}$$

where the superposed dot denotes the derivative with respect to time. The plastic multiplier and the yield function need to fulfill the Kuhn-Tucker loading and unloading conditions as well as the consistency condition (see Supplementary Methods). For details on the theory of elastoplasticity, the reader is referred to[35,36].

The construction of a suitable material model library, i.e., a large catalog of potential candidate models, builds the basis for the unsupervised discovery framework. As the elastic material properties can be identified independently from the plastic material properties in a preprocessing step (for example, based on the full-field measurements of the first load steps, see refs. [31,37]), the elastic stiffness tensor is assumed to be known here and the main focus lies on the discovery of the yield function (see Table 1). The material model library is constructed by choosing a Fourier series ansatz (See refs. [38,39] for other Fourier-type expansions of the yield surface).

$$f(r, \alpha, \gamma) = \sqrt{\frac{3}{2}} r - H^\mathrm{iso}(\gamma) \sum_{i=0}^{n_f} \theta_i \cos(3i\alpha), \tag{2}$$

where $\theta_i$ are the unknown components of the material parameter vector $\boldsymbol{\theta}$ and $(n_f + 1)$ is the number of features in the library. The Lode radius $r$ and the Lode angle $\alpha$ are invariants of the relative stress tensor $\boldsymbol{\sigma}^\mathrm{rel} = \boldsymbol{\sigma} - \boldsymbol{\sigma}^\mathrm{back}$, and are related to the relative principal stresses $\sigma_i$, i.e., the eigenvalues of $\boldsymbol{\sigma}^\mathrm{rel}$, through

$$\begin{aligned} &r = \sqrt{\pi_1^2 + \pi_2^2}, \quad \alpha = \mathrm{atan2}(\pi_2, \pi_1), \quad \text{with} \\ &\pi_1 = \sqrt{\frac{2}{3}}\sigma_1 - \sqrt{\frac{1}{6}}\sigma_2 - \sqrt{\frac{1}{6}}\sigma_3, \quad \pi_2 = \sqrt{\frac{1}{2}}\sigma_2 - \sqrt{\frac{1}{2}}\sigma_3, \end{aligned} \tag{3}$$

where $\mathrm{atan2}(\cdot, \cdot)$ is the four-quadrant inverse tangent and the eigenvalues are taken in increasing order, i.e., $\sigma_1 \le \sigma_2 \le \sigma_3$. Sine terms as well as certain cosine terms are excluded from the library Equation (2) to fulfill isotropy requirements (see Supplementary Methods).

Isotropic hardening is considered in Equation (2) through the nonlinear isotropic hardening function $H^\mathrm{iso}(\gamma)$, whereas kinematic hardening is incorporated by letting the back stress evolve nonlinearly with the plastic deformation. We here assume Voce isotropic hardening[40,41] and Armstrong-Frederick kinematic hardening[42] by defining

$$\begin{aligned} H^\mathrm{iso}(\gamma) &= 1 + H_1^\mathrm{iso}\gamma + H_2^\mathrm{iso}\left(1 - \exp(-H_3^\mathrm{iso}\gamma)\right), \\ \dot{\boldsymbol{\sigma}}^\mathrm{back} &= H_1^\mathrm{kin}\dot{\boldsymbol{\epsilon}}_\mathrm{p} - H_2^\mathrm{kin}\dot{\gamma}\boldsymbol{\sigma}^\mathrm{back}, \end{aligned} \tag{4}$$

where $\mathbf{H} = [H_1^\mathrm{iso}\ H_2^\mathrm{iso}\ H_3^\mathrm{iso}\ H_1^\mathrm{kin}\ H_1^\mathrm{kin}]$ is a vector containing the unknown hardening parameters that are here assumed to be non-negative.

By choosing different combinations of active features in the Fourier series, Equation (2) can be used to describe smooth yield surfaces of arbitrary shape. The representation of the yield function as a closed-form mathematical expression (in contrast to black-box models or constitutive-model-free approaches) facilitates physical interpretation of the material model. E.g., it becomes straightforward to verify whether the yield surface is convex or whether the material behavior is tension-compression symmetric (see Supplementary Methods). The closed-form description also enables interpretable constraints on the parameters $\boldsymbol{\theta}$ based on physical requirements. E.g., assuming a

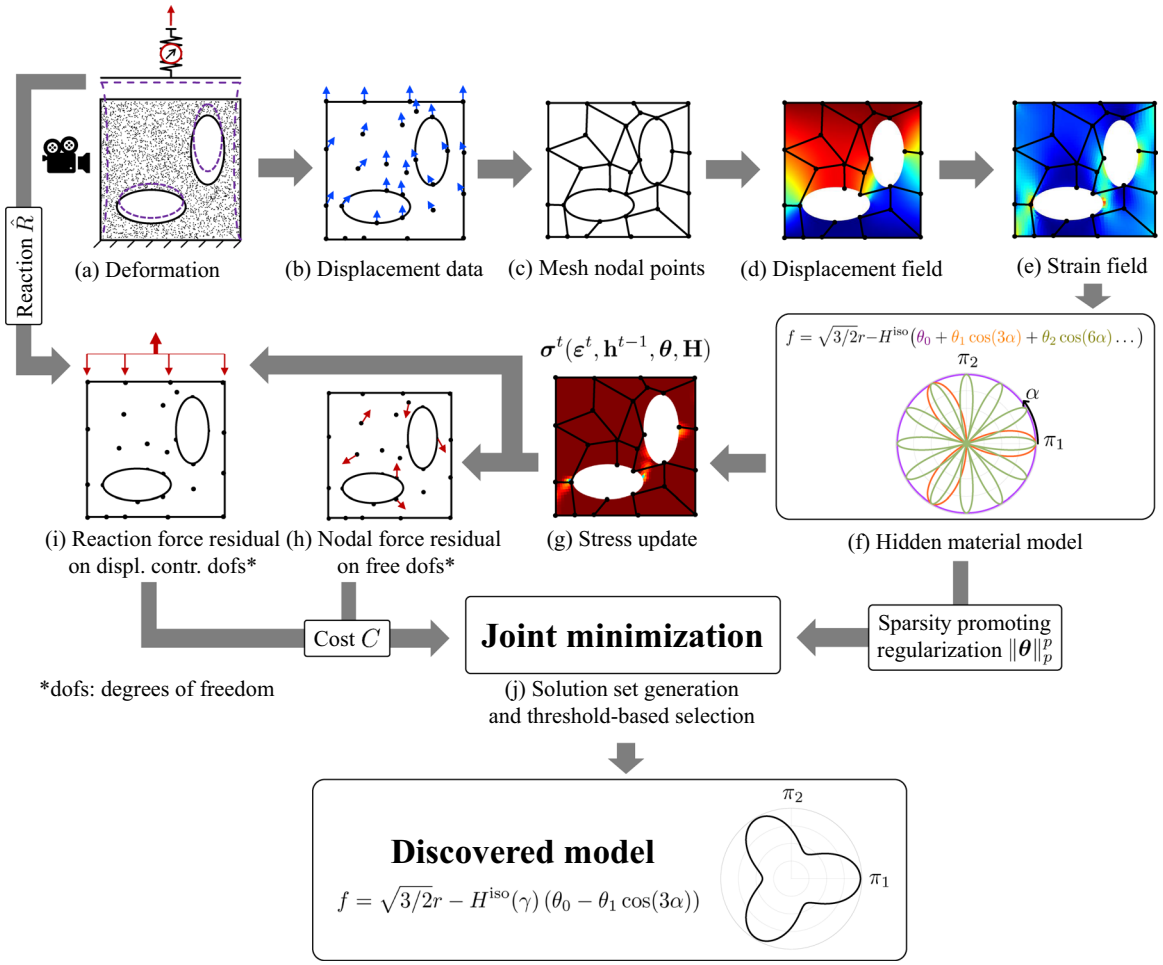


**Fig. 1 Step-by-step schematic of EUCLID.** In a single experiment with complex geometry (**a**), point-wise displacements (**b**), and global reaction forces (**i**) are measured. A quadrilateral finite element mesh is constructed (**c**) to interpolate the displacement data. The resulting displacement field (**d**) is differentiated to arrive at the strain field (**e**). The material model library (**f**) is constructed (here based on a Fourier ansatz). Based on this library and for given material parameters $\boldsymbol{\theta}$ and $\mathbf{H}$, the stresses can be calculated by applying a classical elastic predictor-plastic corrector return mapping algorithm at each load step in the data set, while the history variables are updated at each step (**g**). Based on the stresses, the internal and external virtual works and hence the internal (**h**) and external (**i**) force imbalances are calculated, contributing to the cost function $C$. Finally, the cost function is minimized jointly with a sparsity promoting regularization term (**j**) to generate a set of solutions out of which a solution with low cost and high parsimony is automatically selected. Details are provided in Supplementary Figure 1.

vanishing stress state and that no hardening has occurred ($\boldsymbol{\sigma} = \mathbf{0}$, $\gamma = 0$, $\boldsymbol{\sigma}^{\text{back}} = \mathbf{0}$), the material is expected to behave elastically ($f < 0$),

$$f(\boldsymbol{\sigma} = \mathbf{0}, \gamma = 0, \boldsymbol{\sigma}^{\text{back}} = \mathbf{0}) = f(r = 0, a, \gamma = 0) < 0 \;\Rightarrow\; \theta_0 > \sum_{i=1}^{n_f} |\theta_i|. \tag{5}$$

The numerical implementation of the model library presented in this section, either for forward finite element simulations (used to generate the artificial data) or for the inverse discovery algorithm (EUCLID), requires the formulation of a stress update procedure. Given the strain $\boldsymbol{\epsilon}^t$ at the current time step $t$, the history variables $\mathbf{h}^{t-1} = \{\boldsymbol{\epsilon}_{\text{p}}^{t-1}, \gamma^{t-1}, (\boldsymbol{\sigma}^{\text{back}})^{t-1}\}$ of the previous time step (All history variables are assumed to vanish at $t = 0$, i.e., $\mathbf{H}^0 = \{\mathbf{0}, 0, \mathbf{0}\}$.) and the material parameters $\boldsymbol{\theta}$ and $\mathbf{H}$, the current stress $\boldsymbol{\sigma}^t(\boldsymbol{\epsilon}^t, \mathbf{h}^{t-1}, \boldsymbol{\theta}, \mathbf{H})$ is calculated via a classical elastic predictor-plastic corrector return mapping algorithm (see Supplementary Methods).

### Optimization problem

To compensate for the unavailability of stress data, we employ physics knowledge to identify which features in the feature library should be active and to find the values of the corresponding active parameters within $\boldsymbol{\theta}$ and $\mathbf{H}$. Under quasi-static loading of a two-dimensional domain $\Omega$ with boundary $\partial\Omega$, the linear momentum balance ($\nabla \cdot \boldsymbol{\sigma} = \mathbf{0}$) in its weak formulation is given by

$$\int_\Omega \boldsymbol{\sigma}^t(\boldsymbol{\epsilon}^t, \mathbf{h}^{t-1}, \boldsymbol{\theta}, \mathbf{H}) : \nabla \mathbf{v} \mathrm{d}A = \int_{\partial\Omega} \hat{\mathbf{t}}^t \cdot \mathbf{v} \mathrm{d}s, \tag{6}$$

for all admissible test functions $\mathbf{v}$, where $\hat{\mathbf{t}}^t$ denotes the boundary tractions. The available data consists of displacement measurements $\{\mathbf{u}^{a,t}: a = 1, \dots, n_n; t = 1, \dots, n_t\}$ at $n_n$ points and $n_\beta$ net reaction force measurements $\{\hat{R}^{\beta,t} : \beta = 1, \dots, n_\beta; t = 1, \dots, n_t\}$ on some boundary segments, both for $n_t$ time steps. Our objective is to determine $\boldsymbol{\theta}$ and $\mathbf{H}$ such that Equation (6) is satisfied by the data. We emphasize that, although a two-dimensional inverse problem is formulated here, the discovered plasticity models are valid for three-dimensional stress states. This means that we exploit a two-dimensional data set to automatically find plasticity models applicable to three-dimensional solids.

We create a mesh connecting the points, each point being associated with finite element shape functions $\{N^a(\mathbf{X}): a = 1, \dots, n_n\}$ such that the strain field is obtained as $\boldsymbol{\epsilon}^t(\mathbf{X}) = \sum_a \mathrm{sym}(\nabla N^a(\mathbf{X}) \otimes \mathbf{u}^{a,t})$, and consequently the stress field $\boldsymbol{\sigma}^t(\mathbf{X}, \boldsymbol{\epsilon}^t, \mathbf{h}^{t-1}, \boldsymbol{\theta}, \mathbf{H})$ is

**Table 1.** Yield functions of the (true) hidden and discovered material models ($\gamma = 0$, $\sigma$ in mm, parameters in kN mm$^{-2}$).

| Benchmark | Noise | Yield function $f$ |
|---|---|---|
| VM | Truth | $\sqrt{3/2}r - 0.2400$ |
| | $\sigma = 0$ | $\sqrt{3/2}r - 0.2400$ |
| | $\sigma = 10^{-4}$ | $\sqrt{3/2}r - 0.2437$ |
| | $\sigma = 3 \cdot 10^{-4}$ | $\sqrt{3/2}r - 0.2493$ |
| | $\sigma = 5 \cdot 10^{-4}$ | $\sqrt{3/2}r - 0.2377$ |
| F2 | Truth | $\sqrt{3/2}r - (0.2350 + 0.0050\cos(6a))$ |
| | $\sigma = 0$ | $\sqrt{3/2}r - (0.2350 + 0.0050\cos(6a))$ |
| | $\sigma = 10^{-4}$ | $\sqrt{3/2}r - (0.2349 + 0.0055\cos(6a))$ |
| | $\sigma = 3 \cdot 10^{-4}$ | $\sqrt{3/2}r - (0.2329 + 0.0047\cos(6a))$ |
| | $\sigma = 5 \cdot 10^{-4}$ | $\sqrt{3/2}r - (0.2333 + 0.0041\cos(6a))$ |
| TR | Truth | $\max(\lvert\sigma_1 - \sigma_2\rvert, \lvert\sigma_2 - \sigma_3\rvert, \lvert\sigma_3 - \sigma_1\rvert) - 0.2400$ |
| TR* | Truth* | $\sqrt{3/2}r - (0.2181 + 0.0127\cos(6a) + 0.0035\cos(12a) + 0.0016\cos(18a) + \cdots + 0.0001\cos(60a))$ |
| | $\sigma = 0$ | $\sqrt{3/2}r - (0.2129 + 0.0175\cos(6a) + 0.0033\cos(18a))$ |
| | $\sigma = 10^{-4}$ | $\sqrt{3/2}r - (0.2165 + 0.0184\cos(6a) + 0.0036\cos(18a))$ |
| | $\sigma = 3 \cdot 10^{-4}$ | $\sqrt{3/2}r - (0.2290 - 0.0055\cos(3a) + 0.0208\cos(6a) - 0.0013\cos(12a) + 0.0046\cos(18a))$ |
| | $\sigma = 5 \cdot 10^{-4}$ | $\sqrt{3/2}r - (0.1388 + 0.0106\cos(6a) + 0.0017\cos(12a) + 0.0021\cos(18a))$ |
| SI | Truth | $\max(\lvert\sigma_1 - (\sigma_2 + \sigma_3)/2\rvert, \lvert\sigma_2 - (\sigma_3 + \sigma_1)/2\rvert, \lvert\sigma_3 - (\sigma_1 + \sigma_2)/2\rvert) - \cos(\pi/6)0.2400$ |
| SI* | Truth* | $\sqrt{3/2}r - (0.2518 - 0.0146\cos(6a) + 0.0041\cos(12a) - 0.0018\cos(18a) + \cdots + 0.0002\cos(60a))$ |
| | $\sigma = 0$ | $\sqrt{3/2}r - (0.2260 - 0.0124\cos(6a) + 0.0028\cos(12a))$ |
| | $\sigma = 10^{-4}$ | $\sqrt{3/2}r - (0.2271 - 0.0125\cos(6a) + 0.0028\cos(12a))$ |
| | $\sigma = 3 \cdot 10^{-4}$ | $\sqrt{3/2}r - (0.2374 - 0.0132\cos(6a) + 0.0030\cos(12a))$ |
| | $\sigma = 5 \cdot 10^{-4}$ | $\sqrt{3/2}r - (0.2275 - 0.0130\cos(6a) + 0.0034\cos(12a) - 0.0011\cos(18a))$ |
| F1 | Truth | $\sqrt{3/2}r - (0.2200 + 0.0200\cos(3a))$ |
| | $\sigma = 0$ | $\sqrt{3/2}r - (0.2200 + 0.0200\cos(3a))$ |
| | $\sigma = 10^{-4}$ | $\sqrt{3/2}r - (0.2225 + 0.0199\cos(3a))$ |
| | $\sigma = 3 \cdot 10^{-4}$ | $\sqrt{3/2}r - (0.2177 + 0.0210\cos(3a))$ |
| | $\sigma = 5 \cdot 10^{-4}$ | $\sqrt{3/2}r - (0.1915 + 0.0177\cos(3a))$ |
| IV | Truth | $\max((\sigma_2 + \sigma_3) - 2\sigma_1, (\sigma_3 + \sigma_1) - 2\sigma_2, (\sigma_1 + \sigma_2) - 2\sigma_3) - 0.2400$ |
| IV* | Truth* | $\sqrt{3/2}r - (0.1509 + 0.0415\cos(3a) + 0.0157\cos(6a) + 0.0081\cos(9a) + \cdots + 0.0009\cos(30a))$ |
| | $\sigma = 0$ | $\sqrt{3/2}r - (0.1458 + 0.0417\cos(3a) + 0.0157\cos(6a) + 0.0083\cos(9a) + 0.0048\cos(12a) + 0.0032\cos(15a) + 0.0018\cos(18a))$ |
| | $\sigma = 10^{-4}$ | $\sqrt{3/2}r - (0.1490 + 0.0422\cos(3a) + 0.0165\cos(6a) + 0.0088\cos(9a) + 0.0054\cos(12a) + 0.0029\cos(15a) + 0.0016\cos(18a))$ |
| | $\sigma = 3 \cdot 10^{-4}$ | $\sqrt{3/2}r - (0.1544 + 0.0421\cos(3a) + 0.0160\cos(6a) + 0.0084\cos(9a) + 0.0050\cos(12a) + 0.0025\cos(15a) + 0.0015\cos(18a))$ |
| | $\sigma = 5 \cdot 10^{-4}$ | $\sqrt{3/2}r - (0.1439 + 0.0427\cos(3a) + 0.0181\cos(6a) + 0.0094\cos(9a) + 0.0039\cos(12a) + 0.0018\cos(15a))$ |
| MA | Truth | $\max(\sigma_1 - (\sigma_2 + \sigma_3)/2, \sigma_2 - (\sigma_3 + \sigma_1)/2, \sigma_3 - (\sigma_1 + \sigma_2)/2) - \cos(\pi/3)0.2400$ |
| MA* | Truth* | $\sqrt{3/2}r - (0.3018 - 0.0830\cos(3a) + 0.0315\cos(6a) - 0.0162\cos(9a) + \cdots + 0.0017\cos(30a))$ |
| | $\sigma = 0$ | $\sqrt{3/2}r - (0.1539 - 0.0404\cos(3a) + 0.0146\cos(6a) - 0.0071\cos(9a) + 0.0048\cos(12a) - 0.0034\cos(15a) + 0.0019\cos(18a))$ |
| | $\sigma = 10^{-4}$ | $\sqrt{3/2}r - (0.1574 - 0.0424\cos(3a) + 0.0167\cos(6a) - 0.0083\cos(9a) + 0.0054\cos(12a) - 0.0034\cos(15a) + 0.0017\cos(18a))$ |
| | $\sigma = 3 \cdot 10^{-4}$ | $\sqrt{3/2}r - (0.1641 - 0.0445\cos(3a) + 0.0163\cos(6a) - 0.0074\cos(9a) + 0.0043\cos(12a) - 0.0035\cos(15a) + 0.0023\cos(18a))$ |
| | $\sigma = 5 \cdot 10^{-4}$ | $\sqrt{3/2}r - (0.1664 - 0.0445\cos(3a) + 0.0177\cos(6a) - 0.0092\cos(9a) + 0.0052\cos(12a) - 0.0029\cos(15a) + 0.0018\cos(18a))$ |
| NC | Truth | $\sqrt{3/2}r - (0.1700 + 0.0700\cos(3a))$ |
| | $\sigma = 0$ | $\sqrt{3/2}r - (0.1702 + 0.0699\cos(3a))$ |
| | $\sigma = 10^{-4}$ | $\sqrt{3/2}r - (0.1734 + 0.0638\cos(3a) - 0.0023\cos(6a) + 0.0013\cos(9a))$ |
| | $\sigma = 3 \cdot 10^{-4}$ | $\sqrt{3/2}r - (0.1875 + 0.0615\cos(3a) - 0.0041\cos(6a) - 0.0039\cos(9a) + 0.0052\cos(12a) + 0.0039\cos(15a) - 0.0048\cos(18a))$ |
| | $\sigma = 5 \cdot 10^{-4}$ | $\sqrt{3/2}r - (0.1958 + 0.0457\cos(3a) - 0.0038\cos(6a) - 0.0031\cos(9a) + 0.0109\cos(12a) - 0.0022\cos(15a) - 0.0028\cos(18a))$ |

determined for each time step via the elastoplastic constitutive law described by $\boldsymbol{\theta}$ and $\mathbf{H}$. Using the same set of shape functions for the test functions, the nodal internal forces are computed as

$$\mathbf{F}^{a,t}(\boldsymbol{\theta}, \mathbf{h}) = \int_\Omega \boldsymbol{\sigma}^t(\mathbf{X}, \boldsymbol{\epsilon}^t, \mathbf{h}^{t-1}, \boldsymbol{\theta}, \mathbf{H}) \nabla N^a(\mathbf{X}) \mathrm{d}A. \tag{7}$$

Equilibrium dictates that the internal forces corresponding to all free degrees of freedom (grouped in the set $\mathcal{D}^{\text{free}}$) be zero at each time step, which naturally leads to the cost function

$$C^{\text{free}}(\boldsymbol{\theta}, \mathbf{H}) = \sum_{t=1}^{n_t} \sum_{(a,i) \in \mathcal{D}^{\text{free}}} \left| F_i^{a,t}(\boldsymbol{\theta}, \mathbf{H}) \right|^2. \tag{8}$$

At the same time, for each set of constrained degrees of freedom $\mathcal{D}^{\text{disp},\beta}$, equilibrium requires that the *sum of the internal forces* be balanced at each time step by the corresponding

reaction force $\hat{R}^{\beta,t}$,

$$C^{\text{disp}}(\boldsymbol{\theta},\mathbf{H}) = \sum_{t=1}^{n_t}\sum_{\beta=1}^{n_\beta}\left|\hat{R}^{\beta,t} - \sum_{(a,i)\in\mathcal{D}^{\text{disp},\beta}} F_i^{a,t}(\boldsymbol{\theta},\mathbf{H})\right|^2. \tag{9}$$

We combine the two costs in a single cost function

$$C(\boldsymbol{\theta},\mathbf{H}) = C^{\text{free}}(\boldsymbol{\theta},\mathbf{H}) + \lambda_r C^{\text{disp}}(\boldsymbol{\theta},\mathbf{H}), \tag{10}$$

with the balancing hyperparameter $\lambda_r > 0$. For details, see Supplementary Methods.

The key difference between EUCLID and traditional (supervised or unsupervised) parameter identification methods is the fact that the form of the material model is not known a priori. In the context of yield surface discovery, the number and combination of active features in Equation (2) is unknown. Directly minimizing the cost function in Equation (10) would result in a dense solution vector $\boldsymbol{\theta}$, i.e., a highly complex material model with many non-zero material parameters. Such material models are not desired as their calibration and implementation are impractical and they bear a high risk of overfitting the data, possibly resulting in physically inadmissible material behavior. For these reasons, we promote sparsity in the solution vector by formulating an $\ell_p$-regularized minimization problem as

$$\{\boldsymbol{\theta}^{\text{opt}},\mathbf{H}^{\text{opt}}\} = \arg\min_{\{\boldsymbol{\theta},\mathbf{H}\geq\mathbf{0}\}}\left(C(\boldsymbol{\theta},\mathbf{H}) + \lambda_p\|\boldsymbol{\theta}\|_p^p\right), \qquad \text{where} \qquad \|\boldsymbol{\theta}\|_p = \left(\sum_{i=1}^{n_f}|\theta_i|^p\right)^{1/p} \tag{11}$$

For the hardening models, we assume a mathematical form that is parsimonious at the outset but flexible enough to describe a large class of different hardening mechanisms. To achieve parsimony in the yield surface, we apply $\ell_p$-regularization to the parameter vector $\boldsymbol{\theta}$. The regularization with hyperparameters $\lambda_p > 0$ and $p \in (0, 1]$ is a generalization of the LASSO (least absolute shrinkage and selection operator)[43] which is recovered for $p = 1$. Smaller values of $p$ and higher values of $\lambda_p$ promote sparsity more aggressively, but on the other side increase the degree of the non-convexity of the function to be minimized. Here, as in our previous work[31], we use $p = 1/4$, while the choice of $\lambda_p$ is discussed in the Supplementary Methods. Note that in order to fulfill Equation (5), the parameter $\theta_0$ corresponding to the constant Fourier mode is purposefully not considered in the $\ell_p$ regularization. Further, we highlight that applying the $\ell_p$ regularization shrinks the absolute values $|\theta_i|$ for $i \in \{1, \ldots, n_f\}$ and hence reinforces the fulfillment of the physical constraint in Equation (5). A similar correlation between sparsity of the material model and fulfillment of physical requirements has been observed by[31,34], supporting the hypothesis that sparse models are more likely to fulfill physical requirements.

Equation (11) is a nonlinear and non-convex optimization problem. As there exists no closed-form expression for the stress–strain relation $\boldsymbol{\sigma}^t(\boldsymbol{\epsilon}^t, \mathbf{h}^{t-1}, \boldsymbol{\theta}, \mathbf{H})$, it is not feasible to differentiate the cost function in closed form. For this reason, we use a trust-region reflective Newton solver[44] with gradients computed via a finite difference approximation; however, other optimization techniques may also be feasible to use. To tackle the issue of non-convexity, which leads to multiple local minima, we optimize for multiple randomly chosen initial guesses and operate an automatic threshold-based selection that favors a solution with low cost and high parsimony. All details regarding the optimization procedure are provided in the Supplementary Methods.

## Benchmarks

We benchmark EUCLID on eight largely different elastoplastic material models with different hardening parameters (see Tables 1 and 2 and Fig. 3 for yield function expressions, hardening parameters, and yield surface plots, respectively)[45,46]:

- VM: Von-Mises yield function
- F2: Yield function in Equation (2) with only $\theta_0, \theta_2 \neq 0$
- TR*: Smooth approximation of Tresca yield function[47]
- SI*: Smooth approximation of Schmidt-Ishlinsky yield function[48,49]
- F1: Yield function in Equation (2) with only $\theta_0, \theta_1 \neq 0$
- IV*: Smooth approximation of Ivlev yield function[50]
- MA*: Smooth approximation of Mariotte yield function[51]
- NC: Yield function with non-convex yield surface

The first four material models VM, F2, TR*, SI* exhibit tension-compression symmetry, while the others are tension-compression asymmetric. Material models VM, F2, F1, NC are obtained by choosing different combinations of active and inactive parameters in Equation (2). While yield surfaces in classical plasticity are convex and despite the issues connected with the thermodynamic consistency of non-convex yield surfaces, we deliberately choose model NC to evaluate the capabilities of our approach also in the rare case of non-convexity[52]. The original Tresca, Schmidt-Ishlinsky, Ivlev, and Mariotte models are characterized by non-smooth yield functions which require complex stress update procedures[36] beyond the scope of this work. Therefore, and in order to verify the flexibility of the chosen yield function library, the models with non-smooth yield functions are approximated by the Fourier-type expansion in Equation (2) and denoted by superscript $(\cdot)^*$. Each of the approximated models contains eleven active features with $n_f$ up to 20 in Equation (2), see Supplementary Table 1. The validity of such approximations is proved in the Supplementary Methods.

EUCLID takes full-field displacement and global reaction force measurements as input. DIC data are emulated by generating artificial data via the finite element method (FEM) based on the material models illustrated above. The chosen domain is a square plate with two elliptic holes (as schematically shown in Fig. 2) in-plane stress conditions and meshed with bilinear quadrilateral elements. The plate is deformed under displacement-controlled tension, followed by displacement-controlled compression. In the tension phase, the prescribed vertical displacement $\delta$ is linearly increased from 0 to $\delta = 0.5$ mm, and subsequently decreased to $\delta = -0.5$ mm in the compression phase. The nodal displacements are recorded from the FEM solution at a total of $n_t = 2250$ load steps, 750 load steps in the tension phase, and 1500 load steps in the compression phase. The total horizontal and vertical reaction forces on the top boundary are also recorded. Note that we purposefully choose a complex specimen geometry, in contrast to the simple geometry of traditional coupon tests, with the objective to obtain a strain field that is rich enough to solve the ill-posed problem of identifying the yield surface with no stress data and just one experiment.

As real DIC data are unavoidably affected by noise in the measured displacement field, we add independent Gaussian noise with zero mean and standard deviation $\sigma > 0$ to the synthetic displacement data coming from the FEM simulations (see Supplementary Methods). We consider noise levels $\sigma \in \{0\,\mu\text{m}, 0.1\,\mu\text{m}, 0.3\,\mu\text{m}, 0.5\,\mu\text{m}\}$, where $\sigma = 0.1\,\mu$m is considered a reasonable upper limit for modern DIC setups[53,54]. Pushing EUCLID to its breaking point, we further test it for a noise level of $\sigma = 0.5\,\mu$m. The effect of the noise on the yield surface discovery can be reduced by temporal and spatial smoothing. Here, we restrict ourselves to temporal denoising by applying a Savitzky-Golay filter[55] based on quadratic polynomial fitting with a moving-window length of 50-time steps.

With EUCLID, discovery can proceed from a potentially very large model library—e.g., in our previous work[31] a library with 43 features was used for the discovery of hyperelastic strain energy functions. However, it turns out that with the chosen Fourier ansatz a relatively small number of features is already sufficient to provide a remarkably flexible and general yield surface description. Thus,

**Table 2.** Hardening parameters of the (true) hidden and discovered plasticity models ($\sigma$ in mm).

| Benchmark | Noise | $H_1^{iso}$ | $H_2^{iso}$ | $H_3^{iso}$ | $H_1^{kin}$ | $H_1^{kin}$ |
|---|---|---|---|---|---|---|
| VM | Truth | 40.00 | 2.00 | 900.00 | 150.00 | 600.00 |
| | $\sigma = 0$ | 40.00 | 2.00 | 900.00 | 150.00 | 600.00 |
| | $\sigma = 10^{-4}$ | 39.18 | 2.00 | 846.40 | 148.38 | 626.33 |
| | $\sigma = 3 \times 10^{-4}$ | 38.01 | 1.99 | 778.13 | 155.19 | 650.66 |
| | $\sigma = 5 \times 10^{-4}$ | 39.48 | 1.98 | 958.57 | 171.20 | 678.39 |
| F2 | Truth | 120.00 | 0.00 | 0.00 | 300.00 | 1000.00 |
| | $\sigma = 0$ | 120.00 | 0.00 | 35.46 | 300.00 | 1000.00 |
| | $\sigma = 10^{-4}$ | 121.21 | 1.21 | 5.18 | 294.86 | 1014.55 |
| | $\sigma = 3 \times 10^{-4}$ | 118.65 | 0.02 | 108.71 | 321.29 | 1050.95 |
| | $\sigma = 5 \times 10^{-4}$ | 117.56 | 0.01 | 12003.28 | 323.39 | 1040.07 |
| TR* | Truth | 0.00 | 1.00 | 500.00 | 50.00 | 500.00 |
| | $\sigma = 0$ | 0.00 | 0.98 | 525.88 | 56.52 | 545.59 |
| | $\sigma = 10^{-4}$ | 0.00 | 0.97 | 498.77 | 52.45 | 563.99 |
| | $\sigma = 3 \times 10^{-4}$ | 0.00 | 0.82 | 468.30 | 56.45 | 536.35 |
| | $\sigma = 5 \times 10^{-4}$ | 0.00 | 1.58 | 2859.78 | 74.47 | 579.36 |
| SI* | Truth | 30.00 | 0.50 | 650.00 | 150.00 | 900.00 |
| | $\sigma = 0$ | 30.38 | 0.49 | 570.95 | 140.70 | 813.81 |
| | $\sigma = 10^{-4}$ | 30.14 | 0.51 | 519.93 | 139.01 | 833.54 |
| | $\sigma = 3 \times 10^{-4}$ | 27.39 | 0.50 | 432.26 | 129.30 | 767.45 |
| | $\sigma = 5 \times 10^{-4}$ | 30.79 | 0.45 | 500.98 | 174.01 | 881.25 |
| F1 | Truth | 50.00 | 0.50 | 750.00 | 200.00 | 900.00 |
| | $\sigma = 0$ | 50.00 | 0.50 | 750.00 | 200.00 | 900.00 |
| | $\sigma = 10^{-4}$ | 48.80 | 0.53 | 601.81 | 199.89 | 928.35 |
| | $\sigma = 3 \times 10^{-4}$ | 48.98 | 0.50 | 782.71 | 210.84 | 911.34 |
| | $\sigma = 5 \times 10^{-4}$ | 58.27 | 0.60 | 2321.07 | 218.22 | 894.79 |
| IV* | Truth | 75.00 | 1.50 | 1300.00 | 250.00 | 800.00 |
| | $\sigma = 0$ | 82.61 | 1.66 | 1192.04 | 257.64 | 824.56 |
| | $\sigma = 10^{-4}$ | 78.93 | 1.76 | 1024.17 | 257.66 | 912.86 |
| | $\sigma = 3 \times 10^{-4}$ | 72.88 | 1.68 | 1101.21 | 249.33 | 865.48 |
| | $\sigma = 5 \times 10^{-4}$ | 71.87 | 1.66 | 1380.94 | 255.90 | 838.28 |
| MA* | Truth | 40.00 | 1.50 | 800.00 | 200.00 | 850.00 |
| | $\sigma = 0$ | 41.79 | 1.64 | 861.47 | 191.87 | 845.45 |
| | $\sigma = 10^{-4}$ | 40.26 | 1.58 | 757.54 | 199.24 | 895.49 |
| | $\sigma = 3 \times 10^{-4}$ | 38.38 | 1.50 | 766.04 | 196.12 | 844.04 |
| | $\sigma = 5 \times 10^{-4}$ | 36.34 | 1.46 | 742.06 | 208.52 | 833.68 |
| NC | Truth | 60.00 | 2.00 | 500.00 | 175.00 | 700.00 |
| | $\sigma = 0$ | 59.60 | 2.00 | 498.66 | 174.99 | 694.38 |
| | $\sigma = 10^{-4}$ | 55.93 | 1.85 | 475.22 | 234.90 | 890.36 |
| | $\sigma = 3 \times 10^{-4}$ | 6.44 | 2.24 | 481.16 | 154.28 | 739.98 |
| | $\sigma = 5 \times 10^{-4}$ | 34.26 | 1.95 | 598.01 | 195.75 | 897.60 |

we consider here only seven features ($n_f = 6$) in the model library, i.e., cosine terms with frequencies up to $\frac{18}{2\pi}$. The closed-form expressions of the yield functions discovered by EUCLID from the data with different noise levels are reported in Table 1, in comparison to the true expressions. Table 2 shows the corresponding hardening parameters. A comparison of the yield surface plots in the $\pi$ plane of the true models and the discovered models after hardening ($\gamma = 0.1$) is presented in Fig. 3. As the $\pi$ plane depends on the relative stresses and not on the absolute stresses, the yield surface plots in Fig. 3 do not capture kinematic hardening. To this end, yield surface plots in the absolute stress component space are shown in Fig. 4 for an exemplary material model at the end of three different deformation paths in the data set. Similar plots for the other material models are shown in Supplementary Figures 6 and 7.

In the case of displacements without noise ($\sigma = 0$), material models VM, F2, F1, NC are discovered exactly, i.e., both the mathematical form of the yield function and the parameters are correctly identified. For increasing noise, the discovered parameters deviate from the true parameters as expected. In the non-convex case (NC), false-positive predictions (features that appear in the discovered formula but are not present in the true model) are observed. Material models TR*, SI*, IV*, MA* on the other hand cannot be described exactly by the chosen model library which makes the exact discovery of the yield function form impossible. However, for the tension-compression symmetric models (TR*, SI*)

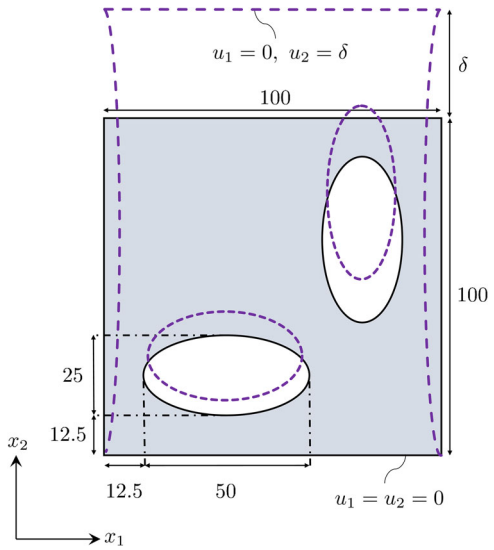


**Fig. 2 Geometry and boundary conditions of the chosen domain: a plate with two elliptic holes under displacement-controlled vertical tension followed by vertical compression.** All dimensions are in mm.

it is observed in many cases that tension-compression symmetry-breaking features (e.g., $\cos(3\alpha)$, $\cos(9\alpha)$ and $\cos(15\alpha)$) are automatically discarded by EUCLID, which increases the interpretability of the discovered models. For the tension-compression asymmetric models (IV*, MA*) the considered ground truth models are not sparse and consequently, EUCLID discovers dense models. This indicates that there is no concise and interpretable model in the library that can describe the provided data accurately. Hence, a trade-off between model accuracy and interpretability is observed in this situation. This could in future studies be mitigated by expanding the feature library, e.g., by including (in addition to the trigonometric features) non-smooth yield surfaces in the ansatz space.

Whenever EUCLID fails to discover the correct yield function form, parameters ($\theta_i$) corresponding to false-positive features are observed to be considerably smaller than the other parameters and hence have a small influence on the material behavior. Further, false-negative feature predictions (features that are not discovered although active in the true model) do not seem to have a high impact on the material behavior either, which is corroborated by the high accuracy observed in the yield surface plots for all models and noise levels except higher noise TR* and NC (see Figs. 3 and 4). Hence, for the models and noise levels for which EUCLID does not find the correct closed-form expression of

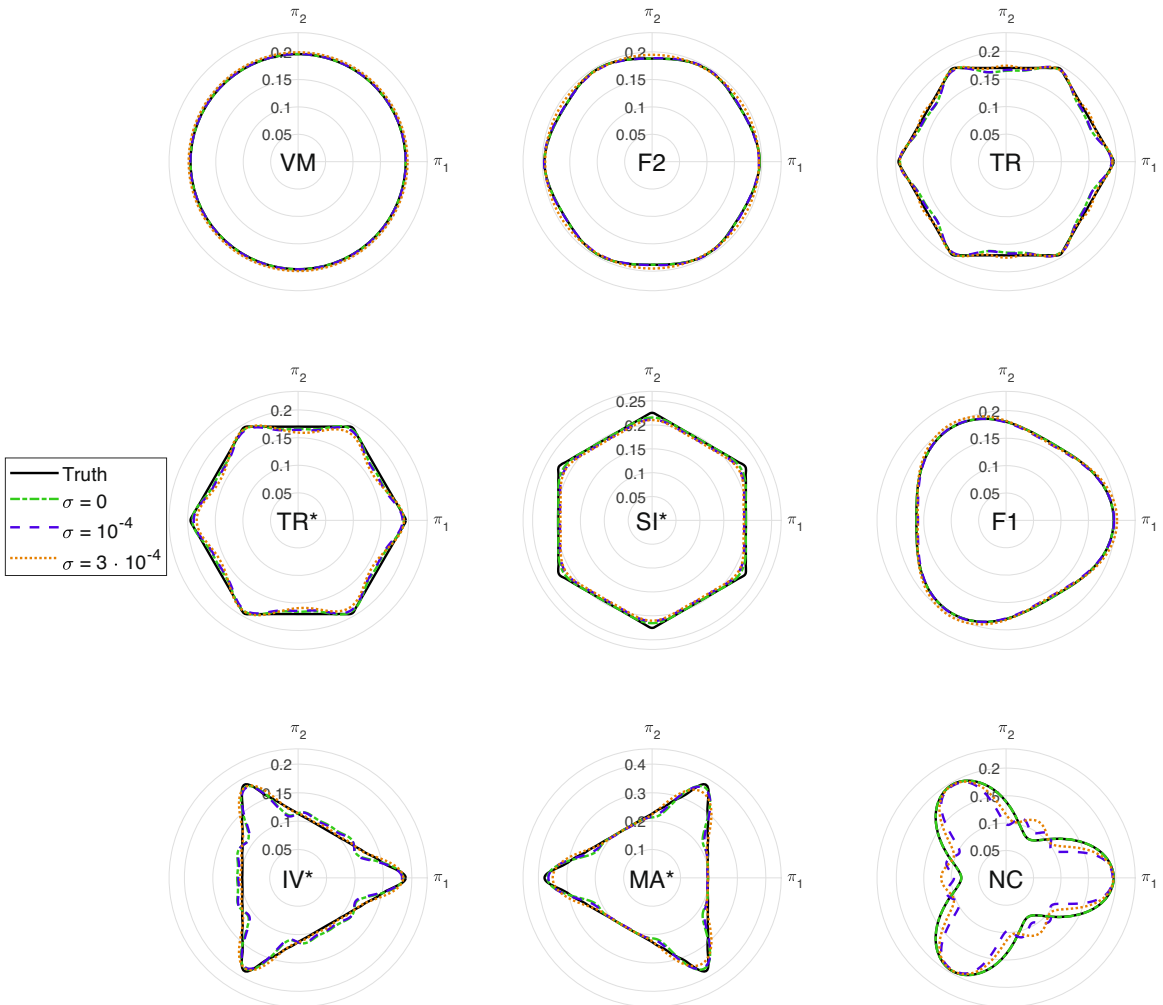


**Fig. 3 Yield surface plots of the (true) hidden and discovered plasticity models for different noise levels $\sigma$ (in mm).** Yield surfaces are shown for $\gamma = 0.1$, which is an upper limit of the accumulated plastic multiplier in the considered data sets. Coordinates $\pi_1$, $\pi_2$ are in kN mm$^{-2}$. For the tension-compression symmetric models, the symmetry axes are indicated by black dotted lines.

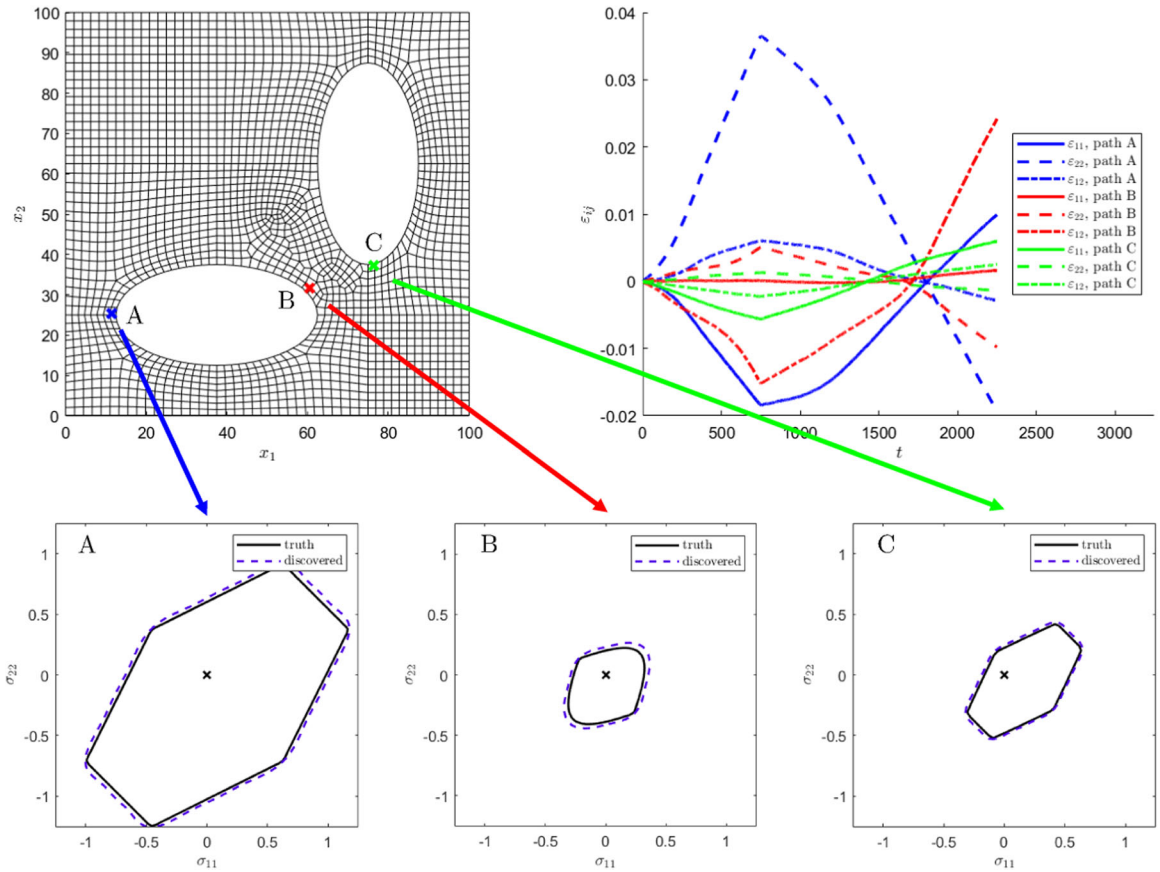


**Fig. 4 Yield surface plots of the (true) hidden and discovered Schmidt-Ishlinsky material model (lower row of plots) at the end of three different deformation paths (A, B, C) corresponding to characteristic points in the specimen domain.** The locations of the points are illustrated in the upper left part of the figure and the strain histories at the different points are shown in the upper right plot. A noise level of $\sigma = 10^{-4}$ mm was considered and the yield surfaces are plotted at $\sigma_{12} = 0$. Coordinates $x_i$ are in mm and $\sigma_{ij}$ are in kN mm$^{-2}$.

the yield function, accurate surrogate models are discovered that mimic the behavior of the true yield function. The Tresca yield surface is the only benchmark for which non-optimal fitting results are observed in shear stress regions even in the case without noise (see Fig. 3). The reasons for this are discussed in detail in the Supplementary Methods, where we also show that enriching the data with shear deformation drastically improves the results.

## DISCUSSION

We show that EUCLID is able to discover interpretable plasticity models from displacement and net reaction force data only and without using any stress data. The method hence provides a physics-constrained, data-efficient alternative to supervised data-driven and machine-learning methods, which require an enormous amount of labeled data and thus are most often inapplicable. The sparse regression enables parsimonious model selection in contrast to an a priori choice of the plasticity model such as in the traditional material model calibration techniques. Hence, after having demonstrated EUCLID for hyperelasticity[31] and for plasticity, we aim at pursuing its extension to the discovery of more general cases of plasticity with pressure sensitivity and anisotropy in future work. Further extensions of interest may include other categories of material behavior such as visco-elasticity, visco-plasticity, damage, and general combinations thereof. Another important future goal will be the employment of EUCLID on experimental data in the two- and three-dimensional settings using digital image and volume correlation data, respectively.

An important question raised by EUCLID is how to choose the specimen geometry and loading conditions to maximize the richness of information in the data. While it is qualitatively clear that more complex setups hold the promise of a richer resulting data set, a quantitative answer requires specific investigations which are an important future research direction. A related question is on the range of strains and loading histories within which the outcome of EUCLID should be trusted. According to our experience, the discovered material model performs accurately not only in interpolation within the range of the data; as EUCLID ensures physical admissibility of the material model, good fitting accuracy, as well as physically sound material behavior, can be observed even beyond the range of the training data. However, as in any other scientific application, extrapolation has its limits and the discovered material model should be used with caution too far outside of the range of the training data set.

## METHODS

Detailed descriptions of the numerical implementation of the material model library, the data generation, the formulation of the objective function, and the optimization procedure are provided in the Supplementary Methods.

## DATA AVAILABILITY

The data generated during the current study are available in the ETH Research Collection[56].

## CODE AVAILABILITY

The codes generated during the current study are available in the ETH Library[57] (see also https://euclid-code.github.io/).

Received: 13 August 2021; Accepted: 14 March 2022;
Published online: 28 April 2022

## REFERENCES

1. Ghaboussi, J., Garrett, J. H. & Wu, X. Knowledge based modeling of material behavior with neural networks. *J. Eng. Mech.* **117**, 132–153 (1991).
2. Sussman, T. & Bathe, K.-J. A model of incompressible isotropic hyperelastic material behavior using spline interpolations of tension-compression test data. *Commun. Numer. Methods Eng.* **25**, 53–63 (2009).
3. Kirchdoerfer, T. & Ortiz, M. Data-driven computational mechanics. *Computer Methods Appl. Mech. Eng.* **304**, 81–101 (2016).
4. Ibañez, R. et al. Data-driven non-linear elasticity: constitutive manifold construction and problem discretization. *Comput. Mech.* **60**, 813–826 (2017).
5. Crespo, J., Latorre, M. & Montáns, F. J. WYPIWYG hyperelasticity for isotropic, compressible materials. *Comput. Mech.* **59**, 73–92 (2017).
6. González, D., Chinesta, F. & Cueto, E. Learning corrections for hyperelastic models from data. *Front. Mater.* **6**, 14 (2019).
7. Mozaffar, M. et al. Deep learning predicts path-dependent plasticity. *Proc. Natl, Acad. Sci.* **116**, 26414–26420 (2019).
8. Zhang, A. & Mohr, D. Using neural networks to represent von Mises plasticity with isotropic hardening. *Int. J. Plasticity* **132**, 102732 (2020).
9. Kovachki, N. et al. Multiscale modeling of materials: computing, data science, uncertainty and goal-oriented optimization. *Mech. Mater.* **165**, 104156 (2022).
10. Leygue, A., Coret, M., Réthoré, J., Stainier, L. & Verron, E. Data-based derivation of material response. *Comput. Methods Appl. Mech. Eng.* **331**, 184–196 (2018).
11. Dalémat, M. Measuring stress field without constitutive equation. *Mech. Mater.* **136**, 103087 (2019).
12. Cameron, B. C. & Tasan, C. Full-field stress computation from measured deformation fields: a hyperbolic formulation. *J. Mech. Phys. Solids* **147**, 104186 (2021).
13. Tartakovsky, A. M., Marrero, C. O., Perdikaris, P., Tartakovsky, G. D. & Barajas Solano, D. Physics informed deep neural networks for learning parameters and constitutive relationships in subsurface flow problems. *Water Resour. Res.* **56** e2019WR026731 (2020).
14. Huang, D. Z., Xu, K., Farhat, C. & Darve, E. Learning constitutive relations from indirect observations using deep neural networks. *J. Comput. Phys.* **416**, 109491 (2020).
15. Haghighat, E., Raissi, M., Moure, A., Gomez, H. & Juanes, R. A physics-informed deep learning framework for inversion and surrogate modeling in solid mechanics. *Comput. Methods Appl. Mech. Eng.* **379**, 113741 (2021).
16. Chinesta, F. et al. Data-driven computational plasticity. *Procedia Eng.* **207**, 209–214 (2017).
17. Ibañez, R. et al. A manifold learning approach to data-driven computational elasticity and inelasticity. *Arch. Comput. Methods Eng.* **25**, 47–57 (2018).
18. Eggersmann, R., Kirchdoerfer, T., Reese, S., Stainier, L. & Ortiz, M. Model-free data-driven inelasticity. *Comput. Methods Appl. Mech. Eng.* **350**, 81–99 (2019).
19. Tang, S. et al. MAP123-EP: A mechanistic-based data-driven approach for numerical elastoplastic analysis. *Comput. Methods Appl. Mech. Eng.* **364**, 112955 (2020).
20. Carrara, P., De Lorenzis, L., Stainier, L. & Ortiz, M. Data-driven fracture mechanics. *Comput. Methods Appl. Mech. Eng.* **372**, 113390 (2020).
21. Carrara, P., Ortiz, M. & De Lorenzis, L. Data-driven rate-dependent fracture mechanics. *J. Mech. Phys. Solids* **155**, 104559 (2021).
22. Li, X., Roth, C. C. & Mohr, D. Machine-learning based temperature- and rate-dependent plasticity model: application to analysis of fracture experiments on DP steel. *Int. J. Plasticity* **118**, 320–344 (2019).
23. Vlassis, N. N. & Sun, W. Sobolev training of thermodynamic-informed neural networks for interpretable elasto-plasticity models with level set hardening. *Comput. Methods Appl. Mech. Eng.* **377**, 113695 (2021).
24. Huang, D., Fuhg, J. N., Weißenfels, C. & Wriggers, P. A machine learning based plasticity model using proper orthogonal decomposition. *Comput. Methods Appl. Mech. Eng.* **365**, 113008 (2020).
25. Shen, W., Cao, Y., Shao, J. & Liu, Z. Prediction of plastic yield surface for porous materials by a machine learning approach. *Mater. Today Commun.* **25**, 101477 (2020).
26. Kumar, S., Tan, S., Zheng, L. & Kochmann, D. M. Inverse-designed spinodoid metamaterials. *npj Comput. Mater.* **6**, 73 (2020).
27. Zheng, L., Kumar, S. & Kochmann, D. M. Data-driven topology optimization of spinodoid metamaterials with seamlessly tunable anisotropy. *Comput. Methods Appl. Mech. Eng.* **383**, 113894 (2021).
28. Hartmaier, A. Data-oriented constitutive modeling of plasticity in metals. *Materials* **13**, 1600 (2020).
29. Bomarito, G. et al. Development of interpretable, data-driven plasticity models with symbolic regression. *Comput. Struct.* **252**, 106557 (2021).
30. Ibáñez, R. et al. Hybrid constitutive modeling: data-driven learning of corrections to plasticity models. *Int. J. Mater. Form.* **12**, 717–725 (2019).
31. Flaschel, M., Kumar, S. & De Lorenzis, L. Unsupervised discovery of interpretable hyperelastic constitutive laws. *Comput. Methods Appl. Mech. Eng.* **381**, 113852 (2021).
32. Flaschel, M., Kumar, S. & De Lorenzis, L. Supplementary software for "Unsupervised discovery of interpretable hyperelastic constitutive laws". *ETH Libr.* https://doi.org/10.5905/ethz-1007-508 (2021).
33. Flaschel, M., Kumar, S. & De Lorenzis, L. FEM Data - Unsupervised discovery of interpretable hyperelastic constitutive laws. *ETH Res Collect* https://doi.org/10.3929/ethz-b-000505693 (2021).
34. Brunton, S. L., Proctor, J. L. & Kutz, J. N. Discovering governing equations from data by sparse identification of nonlinear dynamical systems. *Proc. Natl Acad. Sci.* **113**, 3932–3937 (2016).
35. Simo, J. C. & Hughes, T. J. R. *Computational inelasticity*. No. v. 7 in Interdisciplinary applied mathematics (Springer, New York, 1998).
36. Neto, E. d. S., Peric, D. & Owen, D. *Computational methods for plasticity* (John Wiley & Sons, 2008).
37. Pannier, Y., Avril, S., Rotinat, R. & Pierron, F. Identification of elasto-plastic constitutive parameters from statically undetermined tests using the virtual fields method. *Exp. Mech.* **46**, 735–755 (2006).
38. Ortiz, M. & Popov, E. P. Distortional hardening rules for metal plasticity. *J. Eng. Mech.* **109**, 1042–1057 (1983).
39. Raemy, C., Manopulo, N. & Hora, P. On the modelling of plastic anisotropy, asymmetry and directional hardening of commercially pure titanium: a planar Fourier series based approach. *Int. J. Plasticity* **91**, 182–204 (2017).
40. Voce, E. The relationship between stress and strain for homogeneous deformation. *J. Inst. Met.* **74**, 537–562 (1948).
41. Voce, E. A practical strain-hardening function. *Metallurgia* **51**, 219–226 (1955).
42. Armstrong, P. J. & Frederick, C. *A mathematical representation of the multiaxial Bauschinger effect*, vol. 731 (Central Electricity Generating Board and Berkeley Nuclear Laboratories, 1966).
43. Tibshirani, R. Regression Shrinkage and Selection via the Lasso. *J. R. Stat. Soc.: Ser. B (Methodol.)* **58**, 267–288 (1996).
44. Coleman, T. F. & Li, Y. On the convergence of interior-reflective Newton methods for nonlinear minimization subject to bounds. *Math. Program.* **67**, 189–224 (1994).
45. Kolupaev, V. A. *Equivalent Stress Concept for Limit State Analysis*, vol. 86 of *Advanced Structured Materials* (Springer International Publishing, Cham, 2018). http://link.springer.com/10.1007/978-3-319-73049-3.
46. Rosendahl, P. L., Kolupaev, V. A. & Altenbach, H. Extreme Yield Figures for Universal Strength Criteria. In Altenbach, H. & Öchsner, A. (eds.) *State of the Art and Future Trends in Material Modeling*, vol. 100, 259–324 (Springer International Publishing, Cham, 2019). http://link.springer.com/10.1007/978-3-030-30355-6_12. Series Title: Advanced Structured Materials.
47. Tresca, H. E. *Mémoire sur l'écoulement des corps solides* (Imprimerie impériale, 1869).
48. Schmidt, R. Über den Zusammenhang von Spannungen und Formänderungen im Verfestigungsgebiet. *Ing.-Arch.* **3**, 215–235 (1932).
49. Ishlinsky, A. Y. Hypothesis of strength of shape change (in Russ.: Gipoteza prochnosti formoizmenenija). *Uchebnye Zap. Moskovskogo Universiteta, Mekhanika* **46**, 104–114 (1940).
50. Ivlev, D. The theory of fracture of solids. *J. Appl. Math. Mech.* **23**, 884–895 (1959).
51. Mariotte, E. & de La Hire, P. *Traité du mouvement des eaux et des autres corps fluides* (Chez Claude-Jombert, 1718).
52. Glüge, R. & Bucci, S. Does convexity of yield surfaces in plasticity have a physical significance? *Math. Mech. Solids* **23**, 1364–1373 (2018).
53. Pierron, F., Avril, S. & The Tran, V. Extension of the virtual fields method to elasto-plastic material identification with cyclic loads and kinematic hardening. *Int. J. Solids Struct.* **47**, 2993–3010 (2010).
54. Marek, A., Davis, F. M., Rossi, M. & Pierron, F. Extension of the sensitivity-based virtual fields to large deformation anisotropic plasticity. *Int. J. Mater. Form.* **12**, 457–476 (2019).
55. Savitzky, A. & Golay, M. J. E. Smoothing and differentiation of data by simplified least squares procedures. *Anal. Chem.* **36**, 1627–1639 (1964).
56. Flaschel, M., Kumar, S. & De Lorenzis, L. FEM Data - Discovering plasticity models without stress data. *ETH Res Collect* https://doi.org/10.3929/ethz-b-000534002 (2022).
57. Flaschel, M., Kumar, S. & De Lorenzis, L. Supplementary software for "Discovering plasticity models without stress data". *ETH Lib* https://doi.org/10.5905/ethz-1007-509 (2022).

## ACKNOWLEDGEMENTS

M.F. and L.D.L. gratefully acknowledge the financial support of the Swiss National Science Foundation (SNF Project 200021_204316).

## AUTHOR CONTRIBUTIONS

M.F., S.K., and L.D.L. conceived the research. M.F. developed the theory, implemented the algorithm, and performed the numerical experiments. M.F., S.K., and L.D.L. wrote the paper.

## COMPETING INTERESTS

The authors declare no competing interests.

## ADDITIONAL INFORMATION

**Supplementary information** The online version contains supplementary material available at https://doi.org/10.1038/s41524-022-00752-4.

**Correspondence** and requests for materials should be addressed to Laura De Lorenzis.